Laser-texturing of stainless steel as a corrosion mitigation strategy for high-temperature molten salts applications under dynamic conditions

González-Fernández, Luis; Anagnostopoulos, Argyrios; Karkantonis, Themistoklis; Dimov, Stefan; Chorążewski, Mirosław; Ding, Yulong; Grosu, Yaroslav

DOI:
10.1016/j.solmat.2023.112380

Solar Energy Materials & Solar Cells 257 (2023) 112380

Contents lists available at ScienceDirect

Solar Energy Materials and Solar Cells

journal homepage: www.elsevier.com/locate/solmat

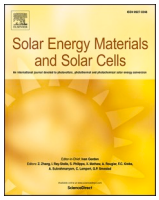

Laser-texturing of stainless steel as a corrosion mitigation strategy for high-temperature molten salts applications under dynamic conditions

Luis González-Fernández [a], Argyrios Anagnostopoulos [b,c,*], Themistoklis Karkantonis [d], Stefan Dimov [d], Mirosław Chorążewski [c], Yulong Ding [b], Yaroslav Grosu [a,c,**]

[a] Centre for Cooperative Research on Alternative Energies (CIC energiGUNE), Basque Research and Technology Alliance (BRTA), Alava Technology Park, Albert Einstein 48, 01510, Vitoria-Gasteiz, Spain
[b] BCES Birmingham Centre of Energy Storage, University of Birmingham, United Kingdom
[c] Institute of Chemistry, University of Silesia, 40-006, Katowice, Poland
[d] Department of Mechanical Engineering, School of Engineering, The University of Birmingham, Birmingham, B15 2TT, UK

A B S T R A C T

Molten salts are utilized in a wide range of applications including nuclear, fuel cells, Carnot batteries, and Concentrated Solar Power (CSP). In order to enhance the profitability of next-generation CSP plants, increasing their efficiency is imperative. Ternary carbonate salts are capable of elevating the maximum CSP operating temperature, which results in improved power generation efficiency. However, higher temperatures lead to accelerated corrosion and more severe conditions for structural materials. In this study, nanosecond laser micromachining is investigated as a potential corrosion mitigation technique for molten carbonate salts in dynamic conditions. SS310 samples with laser-induced surface textures are subjected to the flow of molten Li_2CO_3–K_2CO_3–Na_2CO_3 at 600 °C for a period of 600 h. Laser treatment significantly impedes corrosion in SS310, as untreated samples display pitting and scaling, while minimal surface changes are noted on treated samples. Cross-sectional analysis of the samples reveals considerable peeling in the untreated samples and a 45% increase in the corrosion rate compared to the treated samples. The concentrations of Cr and Mg in the salt (determined through ICP analysis) are found to be twofold and fourfold higher than those in treated samples. Laser treatment renders Cr and Mg less accessible to the salt ions, particularly Li, which results in improved corrosion resistance.

1. Introduction

Fossil fuels account for about 80% of today's world's energy supply. Buildup of greenhouse gases, generated during fossil fuel burning, has resulted in a growing negative environmental trend. An imminent transition to cleaner, renewable, energy technologies is thus necessary to resolve this crisis and pave the pathway to a sustainable net zero society. Solar power is one of the most promising renewable options due to the abundant energy provided by the sun.

Solar energy technologies are categorized into passive and active. The later ones include photovoltaic systems and concentrated solar power (CSP). CSP is a mature technology initially established in the early 1960s. Its first commercial plants were developed in the United States during the mid-1980s (SEGS). However, once the 70s oil crisis was resolved the technology was somewhat abandoned. It has resurfaced in the last couple of decades, initially with a total of 50 government subsidized commercial plant installations in Spain, followed by investment in the United States in the mid-2000s [1]. These were followed by installations in Africa, the Middle East and China. The projected total capacity by 2030 is 204 TWh, up from 14.5 TWh today.

CSP plants concentrate a large area of sunlight onto a small area (receiver) by using mirrors or lenses. This concentrated light is absorbed by a liquid and hence converted into heat. The heat is then used to produce electricity via a Rankine cycle (heat engine). In a typical Rankine cycle, the efficiency depends on the temperature difference between the heat source and sink. Increasing this difference results in an improved efficiency. Current CSP plants typically operate with a mixture of $NaNO_3$–KNO_3 at 60-40 mass ratio, the "so called" Solar Salt (SS). SS has an operating temperature range between ~218 °C (its melting point) and 560 °C (decomposition point) [2].

Typical efficiency for a CSP plants falls in the range between 7 and 25% with a maximum of 60%. This low efficiency coupled with high material and manufacturing costs of the sun tracking system make CSP unprofitable at its current state [3]. To this end, next generation CSP plants are expected to operate at higher temperatures in order to improve the power generation efficiency [4]. Molten salts are well

* Corresponding author. BCES Birmingham Centre of Energy Storage, University of Birmingham, United Kingdom.
** Corresponding author. Centre for Cooperative Research on Alternative Energies (CIC energiGUNE), Basque Research and Technology Alliance (BRTA), Alava Technology Park, Albert Einstein 48, 01510, Vitoria-Gasteiz, Spain.
E-mail addresses: a.anagnostopoulos@bham.ac.uk (A. Anagnostopoulos), ygrosu@cicenergigune.com (Y. Grosu).

https://doi.org/10.1016/j.solmat.2023.112380
Received 16 November 2022; Received in revised form 6 April 2023; Accepted 13 April 2023
Available online 26 May 2023

established in CSP, due to their good heat capacity, high density and low vapour pressure. As such, the best HTF candidates are molten chloride and carbonate salts.

Chloride salts are the most attractive option in terms of pricing but suffer from poor compatibility with CSP structural materials. Corrosion studies report substantially higher degradation of common CSP materials (stainless steel, superalloys) by chloride in comparison to carbonate salts [5]. For this reason, despite their higher price, carbonates are still investigated as a potential candidate. The most explored molten carbonate salt is the ternary carbonate mixture composed of Na_2CO_3–K_2CO_3–Li_2CO_3 (LiNaK) at 33.4 –34.5–32.1 mass ratio. Among others, this ratio is attractive due to a low melting point of ~400 °C. LiNaK has a higher density, specific heat capacity and thermal conductivity than SS and allows for the maximum CSP operational temperature to be extended to 650 °C and 1000 °C in air and CO_2 atmospheres respectively.

Nevertheless, corrosion of structural materials due to LiNaK is also high. Aggressive corrosion has been reported in steel alloys [6–9] as well as superalloys such as Inconel 601 [10]. Lim et al. demonstrated the impact of temperature on the corrosion of SS316L and SS310S in Li/Na carbonates [11], while Frangini et al. confirmed it for Li/K carbonates [12]. Lim et al. also analysed the effect of CO_2/O_2 partial pressure and found that the formation of protective $LiFeO_2$ is hindered by high CO_2 partial pressure, while partial pressure of O_2 has no impact on corrosion [11]. Takeuchi et al. conducted immersion corrosion tests at 650 °C, in a CO_2 atmosphere using Li_2CO_3–K_2CO_3 mixtures, to assess the corrosion resistance of Fe–Cr alloys with different Fe/Cr ratios [13]. The corrosion behavior of SS310 and IN718 in molten Li_2CO_3–K_2CO_3–Na_2CO_3 under CO_2–O_2 atmosphere was systematically investigated by Zhang et al. IN718 exhibited lower corrosion rates compared to SS310, owing to its higher Ni content. Corrosion rates of both materials were reduced by increasing the temperature and decreasing the oxygen concentration [14]. The corrosion behavior of high-chromium ferritic steels and AISI 310 was tested in $(Li_{0.60}/Na_{0.40})_2CO_3$ melt under three cathode gas environments using linear polarization resistance and Tafel extrapolation [15]. Vossen et al. documented the corrosion of several commercially available steels, including SS 310, SS 316, and Kanthal A1, in anodic environments of molten carbonate [16]. A study by M. T. de Miguel et al. [17], investigated the behavior of HR3C austenitic steel in a Li_2CO_3–Na_2CO_3–K_2CO_3 molten salt mixture through a 2000-h isothermal immersion test at 700 °C. The initial-stage corrosion of 310S stainless steel underneath a thin film of molten (0.62Li, 0.38 K)$_2CO_3$ at 650 °C in air has been investigated using electrochemical impedance spectroscopy (EIS) [18]. Luo et al. investigated the corrosion behavior and mechanism of SS316L in the eutectic LiNaK carbonate molten salt, finding that the corrosion process is primarily divided into four successive steps and emphasized on the need to find a good coating in order to enable the use of stainless steels in CSP applications [6]. Sah investigated the corrosion of SS304 in Li_2CO_3–Na_2CO_3–K_2CO_3 at 650 °C and emphasized the importance of evaluating the dissolution of corrosion products as a critical parameter for assessing the performance of construction materials [19]. A detailed presentation of corrosion mechanisms in carbonate salts was recently authored by Bell et al. [20]. Ma et al. recently outlined factors influencing corrosion in molten carbonate salts [21].

To this end researchers have been trying to identify mitigation approaches to improve the corrosion resistance against LiNaK. Quite promising is the use of an alumina slurry, which is applied in the form of a paint on the material surface. Alumina slurry has been shown to improve resistance against carbonate salts on P91 [22]. Another approach was proposed by Fragnini and Loreti, who showcased that addition of Mg, Ca and Ba ions improves corrosion resistance of SS316L in a LiNa carbonate [23]. Nanoparticle doping has also been investigated as a potential mitigation strategy. Literature is, however, contradicting [24]. Carbon steel showed improved corrosion resistance against SS doped with Al_2O_3 or SiO_2 nanoparticles at 1 wt% compared to pure SS [25]. In another work, HitecXL was found to be more corrosive when doped with SiO_2 and Al_2O_3 [26]. Kondaiah and Pitchumani demonstrated reduced corrosion by SS on SS316, In800H, In718, In625, and Ha230 through fractal surface texturing induced by chemical etching [27]. A recent study by Kondaiah and Pitchumani presented multiscale fractal-textured Ni coatings on a variety of substrate alloys that showed good corrosion mitigation in molten ternary carbonate at high temperature, with the corrosion rate reduced by as much as 60% from that of uncoated surfaces [28]. We recently proposed a simple spray graphitization protocol for corrosion inhibition [29]. Graphitization improves compatibility of SS310 and SS347 with molten carbonate salt due to the reaction of the graphite, which results in the formation of carbide layers [30].

However, an issue with these mitigation strategies as well as the literature in general, is that the majority of available studies involve static submersion of an unstressed alloy sample into a molten salt in an isothermal environment for a fixed period [21]. These conditions are not entirely representative of the behavior of molten salts in CSP plants. They only simulate conditions where the salt is idle such as when it is stationary inside the hot or cold tank. Dynamic conditions emulate the movement of the salt in pipes, valves and elbows. These more extreme conditions are quite commonly encountered during operation of a CSP plant in processes such as tank filling or transportation of the salt from one tank to the other. Furthermore, these few existing dynamic condition corrosion studies are mostly focused on nitrate salts [31]. However, they clearly demonstrate that flow conditions can accelerate corrosion. This is because the salt in contact with the metallic surface is constantly refreshed and as such mass transfer and chemical dissolution are enhanced. This, coupled with added flow stress and thermal cycling, increase the degradation rate of the surface [32]. Fernandez et al. [14] reported a higher corrosion rate under dynamic conditions in a molten salt pilot plant operated with $LiNO_3$ ternary molten salt in contact with AISI 316. García-Martín et al. reported higher corrosion rates of A516 after contact with SS at 500 °C for 100h under dynamic conditions with respect to immersion tests [32]. Despite the short timeframe of the test, the aggressive nature of dynamic corrosion was still evident. Zhang et al. found a positive dependence of molten SS velocity and corrosion degradation of SS316 and SS321 at 560 °C [9]. Similar outcomes findings are reported by Ma et al. on the corrosion of SS316L at 565 °C in Ca$(NO_3)_2$–KNO_3–$NaNO_3$–$NaNO_2$. Corrosion rate was found to be highest at 2 m/s and lowest at 0.6 m/s, the highest and lowest tested velocities respectively [33]. Mallco et al. reported that flow accelerated corrosion has a considerably higher impact on the mechanical performance of T91 steel exposed to molten (KLiNa)NO_3 [34]. Audigié et al. [12] examined the anticorrosion performance of two coatings, aluminide and nickel-aluminide, on P91 alloy at 580 °C in contact with SS. Mass gain was found to be much higher in dynamic conditions, with significant spallation, when compared to static ones. Furthermore, a positive relationship was established between salt flow rate and corrosion depth.

We have recently proposed for the first time the use of laser micromachining as a corrosion mitigation approach [35]. Improved corrosion performance of SS310 in contact with LiNaK salt was observed under static conditions. This was due to the considerable reduction of Cr dissolution. In this work, for the first time an investigation of the performance of laser micromachined SS310 under dynamic conditions is presented. Testing the performance of laser micromachined SS310 under dynamic conditions, as presented in this study, is particularly important because there is currently limited research on this topic especially in other corrosion mitigation approaches. Such testing is crucial for determining the feasibility of using this approach for corrosion mitigation in next-generation CSP plants that are expected to operate at higher temperatures for improved efficiency. The successful investigation of laser micromachining under dynamic conditions could provide a solution to the challenge posed by the corrosive properties of molten carbonate salts, paving the way for the development of more efficient and cost-effective CSP plants, which are crucial for advancing

sustainable and net-zero energy goals.

2. Methodology

2.1. Materials and preparation

Eutectic ternary carbonate salt was employed for the corrosion test: 34.5% K_2CO_3 - 33.4% Na_2CO_3 - 32.1% Li_2CO_3 (weight concentration). The components of the ternary salt were purchased from Sigma-Aldrich, with purities higher than 99%. Before mixing in the correct proportions, the carbonates were dried at 120 °C in the oven for no less than 12 h. Afterward, they were weighted and blended.

The samples and the rods, used to transmit the rotational movement from the engine to the sample, were made of SS310. The chemical composition of this stainless steel is detailed in Table 1.

As it can be seen in Fig. 1, a cross-shaped samples with 4 petals were employed in the tests. The samples were cut from a SS310 sheet having 2 mm thickness. The total length of the cross was approximately 70 mm, while the size of the 4 square-shaped petals was 22 mm. In order to facilitate the analysis of the samples after the corrosion test by separating the 4 petals of the cross, the junction between each petal and the central region was reduced to 6–7 mm. A central hole was bored and threaded in the sample to attach it to the SS310 rod by screwing.

Both surfaces of the samples were polished up to 1200 SiC sandpaper using ATM Saphir stationary polishing machine. Next, the samples were successively cleaned in acetone, ethanol and distilled water in an ultrasonic bath for 15 min for each solvent.

2.2. Corrosion protocol and experimental setup

For carrying out the dynamic test, a dedicated setup was developed, which is described elsewhere [26] and is demonstrated in Fig. 2.

The movement is produced by an electric motor located above the furnace and connected to the SS310 rod by a Teflon junction. Teflon was chosen to avoid any electrical connection between the sample and the motor that could have an influence on the corrosion process. The rod enters into the furnace through a hole in its top part. The bottom extreme of the rod is threaded in the way that the sample can be attached by screwing. With this configuration, spinning the sample intends to mimic the dynamic corrosion conditions produced in the inner walls of pipes due to molten salt pumping.

During the test, since the SS310 sample was screwed to the rod, the rotation without touching either the wall or the bottom part of the alumina crucible was ensured. A total mass of 685 g of carbonate salt was employed to ensure that the samples were completely immersed during the experiment. The test was carried out at a spinning rate of 60 rpm, which means a lineal velocity of ~0.2 m/s in the central part of the petals. This velocity is comparable to the range of fluid velocities near to pipe bends and valves in the CSP plants, 0.2–0.5 m/s [37,38]. To ensure that the results were not influenced by a difference in the salt velocity, the analysis were restricted to the region of the petals that corresponds to a linear velocity of (0.20 ± 0.02) m/s. Especially for the cross-section characterization.

When the setup was completely assembled, the furnace was heated to 450 °C in air atmosphere with 5 °C/min heating rate and without rotating the sample. Then, 1 h under isothermal conditions was maintained to ensure that salt entirely melts. Later, the salt was heated to 600 °C at the same heating rate. When the desired temperature was reached, the motor was turned on and the temperature was maintained for 600 h, followed by a cooling step to 450 °C at 5 °C/min and recovery of the sample while the salt is in the molten state.

Two types of samples were tested: Reference sample (Fig. 1, left) and LTS sample (Fig. 1, right).

The 4 petals of the sample were cut from the central part, before cleaning the salt remaining on their surface, with a Struers Miniton precision cutting machine, equipped with a diamond blade. Thus, the outer salt coverage acts as protection during the cutting process. Afterward, the remaining salt was cleaned with distilled water. Anyway, to ensure that the cutting does not affect the later analyses, the sample characterization is carried out avoiding the region affected by the process.

Table 1
Chemical composition (wt%) of tested SS310.

Element [−]	Fe	Ni	Cr	Mn	Si	P	C	S
Mass fraction [%]	Balance	19.1	24.9	1.81	0.64	0.03	0.05	0.01

2.3. Laser surface texturing

The surface texturing experiments are conducted on a laser micromachining workstation, namely LASEA LS5, under ambient conditions. The laser processing setup utilized in this research was identical with that reported already in our previous work [35]. In brief, the system is equipped with a nanosecond MOPA-based Yb fibre laser (SPI G4 S-type) that has the following technical specification: a nominal wavelength of 1064 nm, maximum average power of 50 W and pulse repetition rates up to 1 MHz. Furthermore, a telecentric lens with focal distance of 100 mm and a quarter waveplate (λ/4) were integrated into the beam delivery sub-system. The SS310 samples were processed with a circularly polarised Gaussian beam ($M2 < 1.3$) with a spot diameter of 40 μm at 1/e^2. while the pulse duration was 220 ns. A galvo scan head (Rhothor RTA) was employed to steer the focused laser beam across the substrates at a constant scanning speed of 1000 mm/s.

A stack of three linear motorised stages was employed to accurately position the samples inside the machine's working envelope. The SS310 substrates were irradiated with a fixed pulse repetition rate of 65 kHz and fluence of 9 J/cm^2. Two different surface patterns were produced onto the SS310 substrates in this research, i.e. channel- and grid-like patterns. The channel-like pattern was produced through raster scanning with five passes and the step-over between two scan lines was 100 μm. Regarding the grid-like pattern, it was produced through intersecting scan lines with the same step-over of 100 μm between them and five passes, again. Due to the thermal processing regime during laser texturing process, a recast was formed along the edges of the beam scan lines in both directions that led to the formation of highly uniform square-shaped micropillars on the surface. The mechanism behind the formation of such structures has been described by other researchers [39,40].

2.4. Characterization techniques

2.4.1. Scanning electron microscopy - SEM

For the SEM analysis, a Quanta 200 FEG model was used in high vacuum mode at 20 kV with backscattered electron detector (BSED) and Everhart-Thornley Detector (ETD). Energy-Dispersive X-Ray Spectroscopy (EDX) was performed for elemental mapping.

Firstly, the surfaces of all the samples were analysed by both sides. Secondly, the cross-section of samples was checked to analyse further the corrosion layer. For this purpose, the samples were embedded in a resin holder composed of Aka-Resin and Aka-Cure catalyst (1 ml–0.135 ml proportion, respectively). When the resin solidifies, it creates a hard shell that protects the corrosion layer from detaching during the cutting and polishing processes. To properly observe the sample's cross-section, the samples underwent progressive polishing with 240, 400, 800, 1200 and 2500 SiC sandpaper using an ATM Saphir stationary polishing machine.

2.4.2. X-ray diffraction - XRD

The X-ray diffraction measurements were carried out by means of a

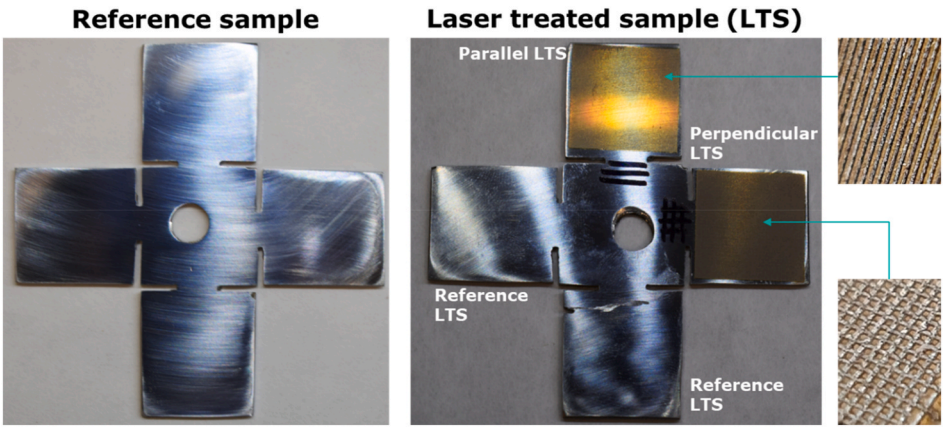

Fig. 1. Photos of reference and laser treated samples for dynamic corrosion tests.

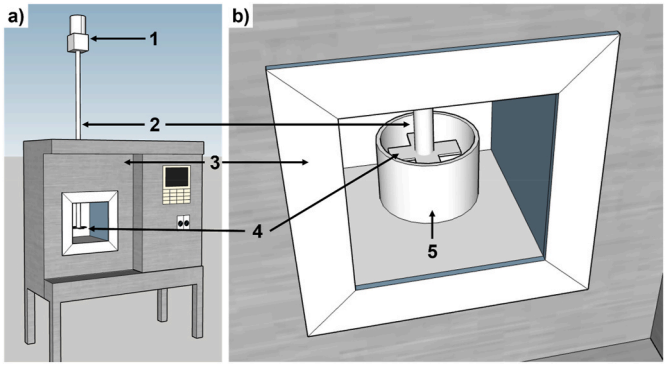

Fig. 2. Schematic view of the experimental setup for dynamic corrosion tests [36]: (1) electric motor, (2) rotation-transmitting SS310 rod, (3) furnace, (4) SS310 sample and (5) alumina crucible.

Bruker D8 Discover X-ray diffractometer equipped with a LYNXEYE detector using CuKα1 radiation (λ = 1.5418 Å) in Bragg-Brentano θ:2θ geometry. The data collection was carried out at room temperature, between 10° and 80°, with a step size of 0.02° and a collection time of 1s/step. Later, the phase identification of each sample was performed by EVA software.

2.4.3. Inductively coupled plasma optical emission spectroscopy – ICP-OES

Samples were analysed using a Horiba Ultima 2 (Jobin Yvon, Longjumeau, France) in conjunction with a AS500 autosampler and Activanalyst software (version 5.4).

The preparation of the samples was carried out by dissolving 0.5 g of the corresponding salt in 25 ml of a solution of 2% of HNO_3.

The ICP-OES operating conditions were as follows: 1.0 kW of RF power, 13 l/min of a plasma-gas flow rate, 0.2 l/min of a sheath-gas flow rate and 0.25 l/min of a nebulizer-gas flow rate. Solutions were introduced into the plasma torch using nebulizer and a cyclonic type of spray chamber at a flow rate of 0.87 ml/min.

A multi-elemental standard solution of 100 mg/l containing 25 elements supplied by Scharlab (Barcelona, Spain) was used for calibration. HNO_3 69% from Scharlab (Barcelona, Spain) analytical grade and Ultrapure Water from Fischer Scientific (Waltham, Massachusetts, USA) were used for dilutions.

The following analytical lines were selected for measurements: Al 396.152 nm, As 193.695 nm, Ba 413.066 nm, Be 249.454 nm, Bi 190.178 nm, Ca 317.933 nm, Cd 226.502 nm, Co 238.892 nm, Cr 267.716 nm, Cu 327.396 nm, Fe 259.940 nm, K 769.896 nm, Li 670.784, Mg 279.079 nm, Mn 257.610 nm, Mo 204.598 nm, Na 589.592 nm, Ni 216.556 nm, Pb 283.306 nm, Se 196.026 nm, Sr 216.596 nm, Ti 336.121 nm, Tl 190.800 nm, V 310.230 nm, Zn 206.191 nm.

3. Results

Exposure of SS310 to molten salt under dynamic conditions, as described in this study, has a significant effect on the material's surface, as illustrated in Fig. 3. The unprocessed reference LTS samples suffered extensive damage, evident from the scaling observed. This damage is even more pronounced in the case of the reference sample, which has several holes on its surface. On the other hand, the processed sample demonstrated effective corrosion mitigation, as evidenced by its uniform structure and absence of significant defects. In fact, small defects were only noticeable on the edges of the sample, which further highlight the corrosion mitigation capabilities of laser micromachining. This is supported by SEM snapshots of the edges of the LTS samples, which were not patterned and therefore demonstrated corrosion features similar to those of the reference cases, as shown in Fig. 3.

Upon observation of the metal surface, it is evident that exposure to molten salt under dynamic conditions has a more significant impact on the surface of SS310 (Fig. 4). In both the reference and reference LTS samples, a high degree of spallation is noticeable. This spallation appears to be due to the molten salt's ability to penetrate the oxide layer and corrode the metal surface beneath. The reference sample shows numerous small pits, while the reference LTS sample has fewer but larger pits between scales. On the other hand, both parallel and perpendicular LTS samples demonstrate almost entirely intact surfaces, with their uniform patterning well-maintained compared to the preprocessing stages (Fig. 4).

A closer look at the reference sample shows the pits in the shape of cracks, positioned in the center of a shape resembling a bursted bubble (Fig. 4). These pits contribute to inhomogeneity on the metal surface, leading to an increase in surface area, thus making chemical species more accessible to salt ions [41]. This increased susceptibility to dissolution results in further degradation. In addition, the irregularities and cracks in the surface can create stress concentrations, which can further accelerate the corrosion process. Corrosion often starts at locations of high stress or strain, where the metal is already weakened, and then spreads from these locations. However, these bubbles are absent in the reference LTS sample, where instead, a high degree of scaling is noted at a higher magnification, indicating high levels of inhomogeneity on multiple scales (Fig. 4).

Remarkably, both parallel and perpendicular laser-treated surfaces appear largely unscathed even at higher magnifications. Small dislocations are evident on the top of the grooves, particularly in the case of the parallel surface, but overall, the surfaces are uniformly covered with a layer of crystals. In fact, zooming in at the 250 μm scale confirms this, with only one particle size evident on the LTS samples as well as a

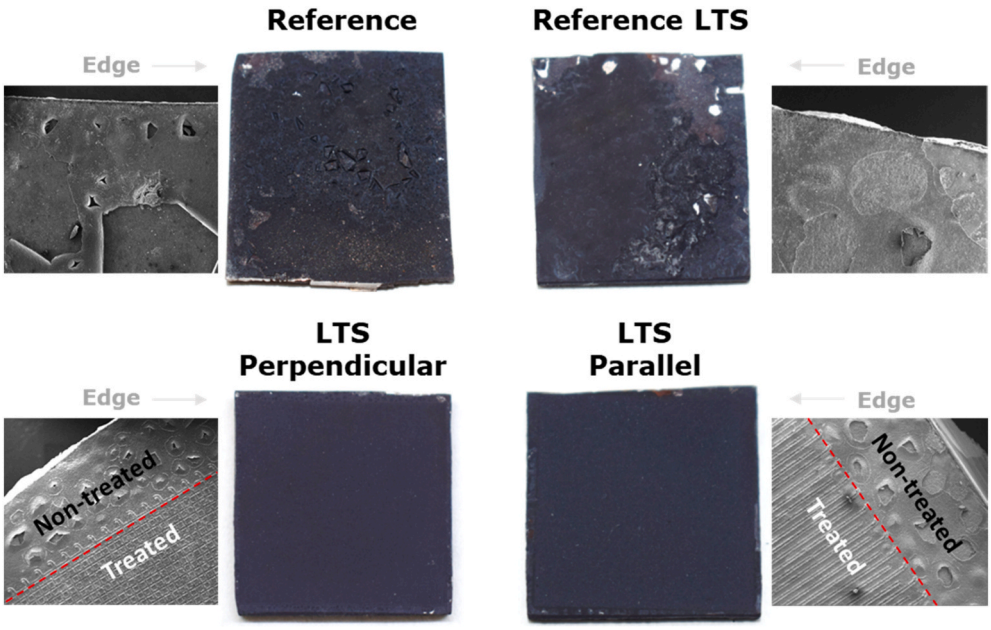

Fig. 3. Photos of SS310 samples after the corrosion test.

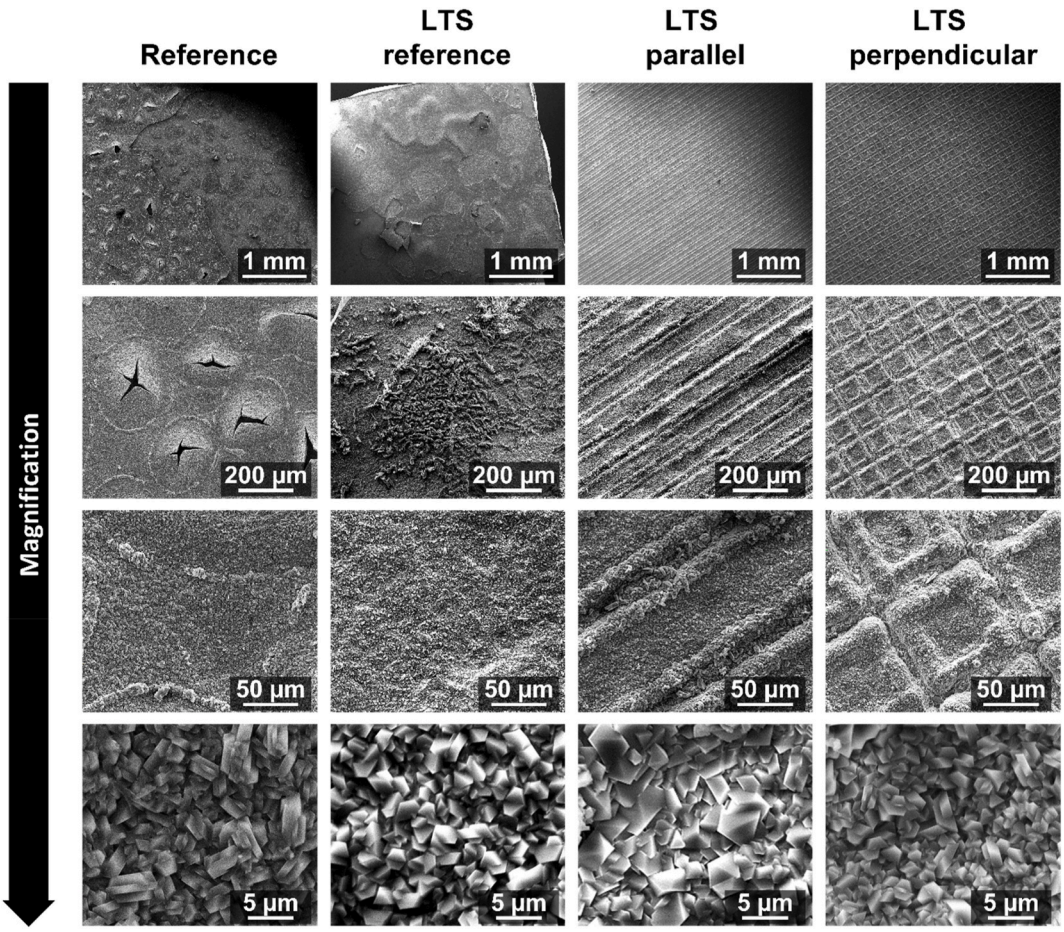

Fig. 4. SEM images of SS310 samples after the corrosion test.

uniform grain structure. However, the reference samples have more than one particle size, suggesting a high degree of scaling.

In the diffractograms of the reference sample, we observe a high intensity of iron and nickel oxide peaks, as seen in Fig. 5. The LTS samples display similar diffraction patterns, except for the peak at the 52° range. This peak corresponds to higher oxidation states of Fe [42], indicating more aggressive diffusion of Fe ions at the interface, which was also observed in the cross-sectional analysis. Additionally, we

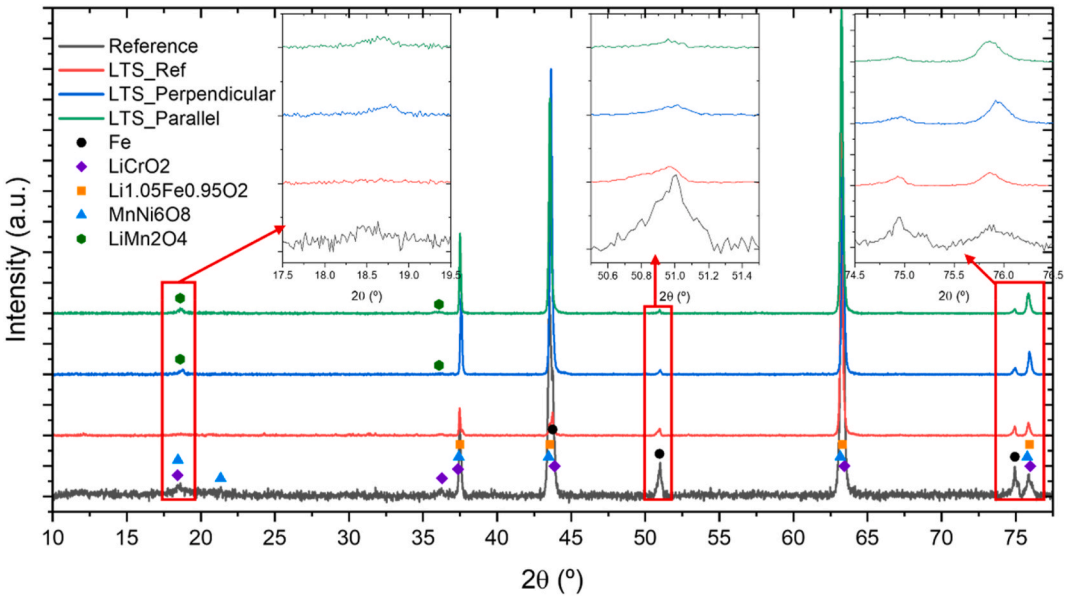

Fig. 5. XRD patterns for SS310 samples after corrosion tests.

observe peaks that correspond to $LiCrO_2$, which suggests outward diffusion of Cr ions. These peaks could also be due to cracking, which reveals areas below the interface where Li ions have diffused. Maintaining the interface of the metal with the molten salt is important to prevent corrosion, and the outward diffusion of ions from the metal can be an indication of corrosion. It appears that laser micromachining is able to mitigate the diffusion of ions at the interface, as evident by the lower intensity of the Fe and Ni oxide peaks in the LTS samples.

The formation of the Li mixed oxides; $LiCrO_2$, $Li_{1.05}Fe_{0.95}O_2$ and $LiMn_2O_4$; can be described according to the reactions (1), (2) and (3) respectively [8,36]:

$$Cr_2O_3 + Li_2CO_3 \rightarrow 2LiCrO_2 + CO_2$$

$$Fe_2O_3 + Li_2CO_3 \rightarrow 2Li_{1.05}Fe_{0.95}O_2 + CO_2$$

$$2Mn_2O_3 + Li_2CO_3 \rightarrow 2LiMn_2O_4 + CO$$

Cross-sectional analysis further verifies this (Fig. 6). The outermost layers of the coating appear to be almost detached for reference and LTS reference samples. This is due to the difference in the thermal expansion of the various corrosion products [18]. This can result in cracking, which reduces mechanical stability and increases the probability of detachment (peel-off). This cracking and detachment is further amplified by the rotational forces subjected to the sample during dynamic testing. These reduce the critical depth, after which it can no longer adhere to the surface.

Such cracking is observed due to the formation of an inner layer of chromium oxide before a mixed nickel-iron oxide layer (Fig. 7). The formation of this double layered structure and its cracking has been previously reported in the literature [43,44]. Iron being the primary constituent of the SS310 is more accessible to the molten salt and thus forms the first corrosion layer. Oxygen present in the air as well as the carbonate salt result in fast oxidation of the metallic components at high temperatures. Selectivity of the highly active elements in SS310 leads to an enrichment of nickel just below the outermost corrosion layer consisting of iron. The reactivity of molten salt components with SS310 is in the order of Li > Na > K [35]. As such, oxidation is followed by a slower lithanation process, which gradually deteriorates the surface of the steel resulting in vacancies in the alloy subsurface. This leads to a flux of ions to the alloy surface by inverse Kirkendall effect [45]. Cr has the highest self-diffusivity and thus replaces most of this space [46]. This increases its contact with the molten salt and its probability of reaction. It has been suggested that iron and manganese form a negative solubility gradient instead of a positive gradient like chromium [47]. This is also in agreement with the corrosion resistance of common alloy elements in

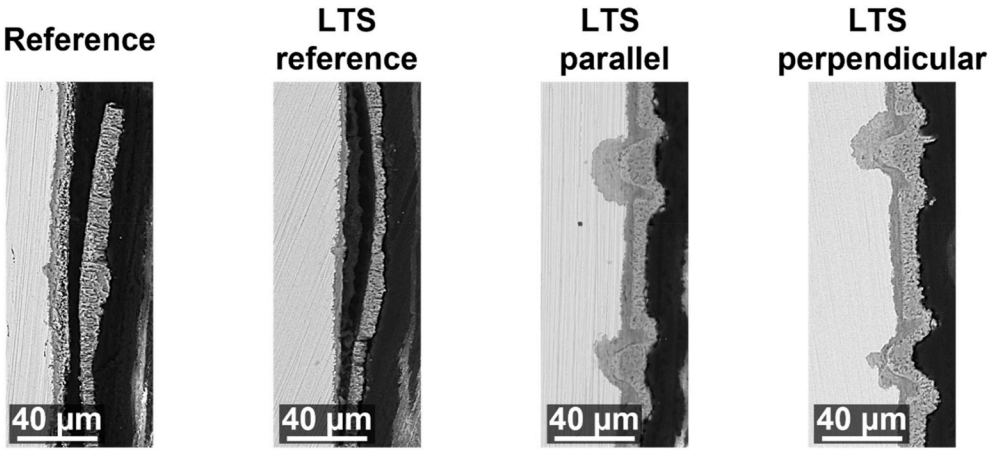

Fig. 6. Cross-sections for SS310 samples after the corrosion tests.

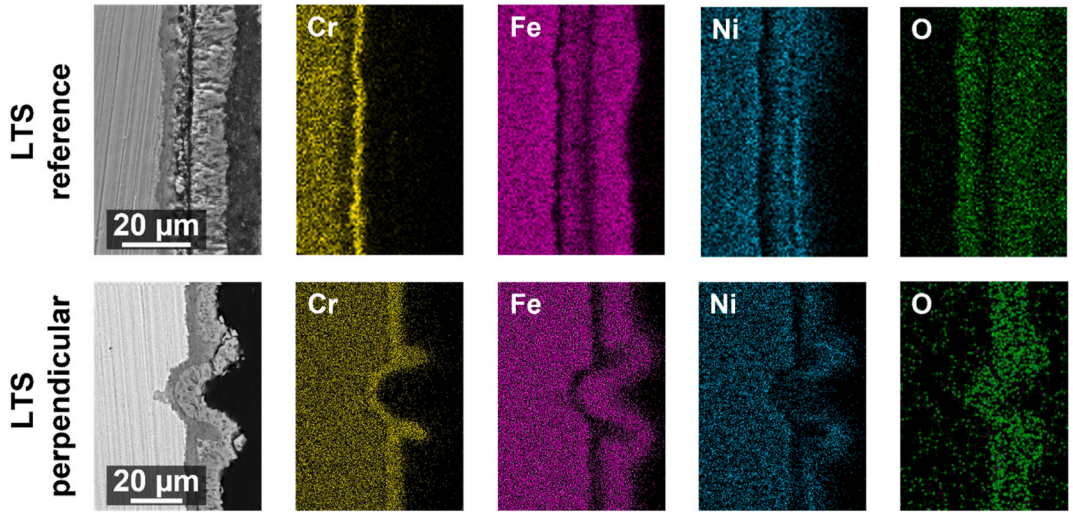

Fig. 7. Cross-sections and EDX-mapping for SS310 samples after the corrosion tests.

molten salts is of the order of Cr < Fe < Ni. This much higher solubility of Cr oxide compared to iron oxide leads to its rapid depletion. This high Cr oxide solubility has been previously confirmed in chloride and nitrate melts [48,49]. Dissolution of chromium oxide in the molten salt is known to increase its basicity, which can then further amplify corrosion. As Fe^{3+} ions continue to diffuse outward and O_2- and Li^+ ions diffuse inward, at faster rates, the thickness of both the outer and inner layers of the oxide scale gradually increases with testing time. As the thickness of the oxide layer reaches a certain value, a crack appears between the outer and inner layers due to a difference in their thermal expansion coefficients. Ultimately, the outer oxide layer becomes fully detached. Dynamic conditions amplify this.

Contrary to the reference sample, LTS exhibit a compact structure primarily composed of iron and nickel oxide, as depicted in Fig. 7. The corrosion layer structure plays a critical role in the corrosion process, where the mass transport process through the corrosion layer likely controls the corrosion rate. At least two distinct layers are present on the surface. The outer layer is considerably thicker and has large oxide grain size and significant porosity, while the sub-chromium oxide layer, approximately 4 μm in thickness, is quite compact with only small levels of porosity.

Type 310 steel, due to its high chromium content, forms a corrosion-resistant layer primarily composed of a thin, compact layer of $LiCrO_2$, which strongly inhibits iron diffusion and hinders the growth of the external $LiFeO_2$ layer. The stability of the latter layer is crucial for the material's passivity. Additionally, nickel oxide, which has the least solubility in molten salt, reduces the dissolution of chromium. Sah et al. reported that Cr and Ni promote corrosion resistance in 310S, 316L, and 304 in contact with carbonate molten salt [50].

Laser texturing can result in the adhesion of long-chain hydrocarbons onto the steel surface [35], and that these hydrocarbons decompose into carbon at higher temperatures, depending on their length [51,52]. This in turn can lead to the formation of protective layers of carbides and carbonates, which stabilize the corrosion process. Additionally, the reaction releases CO_2, which further contributes to the stabilization of the corrosion process. This mechanism is similar to one reported in spray graphitization, which is a technique we recently proposed involving the application of a graphite coating onto a metallic surface to improve its corrosion resistance [53].

The adhesion of long-chain hydrocarbons onto the steel surface during laser texturing is likely due to the thermal effects of the laser, which can cause the surface to become heated and to interact with the surrounding environment. The exact mechanisms of adhesion are still an active area of research, but it is thought that the hydrocarbons become physically and/or chemically bound to the steel surface [54].

The formation of protective carbide and carbonate layers is an important aspect of corrosion resistance in steel [55]. These layers can act as a barrier to prevent the penetration of corrosive species into the underlying steel, and can also help to prevent the growth of existing corrosion pits [56].

Unfortunately, the carbon layer detected via EDX under static conditions may be too thin to observe under dynamic conditions [35]. This suggests that the formation of a thick carbon-containing layer is difficult. Nevertheless, the formation of this layer is a competitive reaction to oxidation, which can result in a lower corrosion rate. This is supported by the SEM results showing high spallation and significant thickness increase (scaling) in the reference and LTS reference cases.

Although challenging due to the non-uniformity of the metallic surface and pronounced spallation, the corrosion rate was determined through image analysis using ImageJ, and was found to be 0.311 ± 0.1 mm/year for the perpendicular LTS configuration, compared to 0.496 ± 0.04 mm/year for the LTS reference case. This indicates that the reference case exhibits a 45.9% higher corrosion rate compared to the LTS perpendicular configuration. The corrosion rate obtained for the reference case is consistent with previously reported data for static corrosion tests, which typically range between 73 μm/year and 438 μm/year. However, it should be noted that this does not account for any potential peel off, which is highly anticipated in such a high-stress environment. Notably, this peel-off is observed in both cross-sectional analysis and SEM imaging. The reduced corrosion rate can be attributed to the replenishment of salt ions near the surface due to mixing during dynamic testing.

The observed significant peel-off in the laser micro-processed samples underscores the criticality of conducting corrosion testing under dynamic conditions to accurately assess the effectiveness of the corrosion inhibition methodology. Notably, under static conditions, the impact of laser micro-processing on corrosion inhibition is less apparent than that of untreated samples [35]. However, the potential of laser micro-processing to inhibit corrosion is more apparent under dynamic conditions, where the aggressive structural degradation of the untreated surface is clearly evident.

This passivation mechanism is further substantiated by the ICP analysis presented in Fig. 8, which reveals that the concentration of Cr in the molten ternary salt is nearly double in the reference samples as compared to those treated with laser surface texturing (LTS). On the other hand, the concentration of magnesium is found to be almost four times higher in reference samples Table 2. While magnesium dissolution can potentially benefit the steel's stability [57], the mixing of the salt

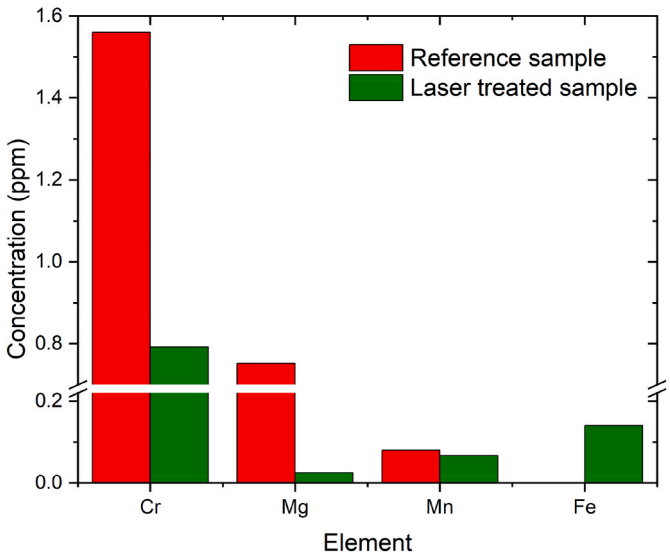

Fig. 8. ICP analysis of molten salts after the corrosion tests.

under dynamic conditions results in Mg ions being uniformly dispersed in the solution, rather than being retained in the vicinity of the salt-steel interface where they could play a helpful role by interacting with the salt or the iron oxide and forming stable compounds [58,59]. This, in conjunction with the substantial degree of Cr diffusion, appears to lead to a considerably aggressive corrosion in the reference case. As previously mentioned, the dissolution of chromium expedites the degradation of the surface by accelerating the thermal decomposition of the salt via its effect on the pH balance [60]. Therefore, inhibiting Cr dissolution through laser treatment seems to be the critical factor in enhancing the corrosion resistance. It should be noted that a second ICP analysis is conducted on the pure salt and no traces of any of these elements is identified. This suggests that any impurities existing in the salt were introduced during the corrosion experiment. Furthermore, we would like to highlight that in previous corrosion experiments under static conditions, no Cr content was detected in the salt when laser-texturized samples were used in the same blend of carbonates salt [61]. Therefore, we are confident that the Cr present in the salts used in this study is a result of its dissolution due to enhanced corrosion under dynamic conditions, rather than due to impurities in the salt.

4. Conclusions

In this study, the effectiveness of nanosecond laser micromachining as a corrosion mitigation technique for SS310 in contact with K_2CO_3–Na_2CO_3–Li_2CO_3 molten carbonate salt under dynamic conditions was investigated. The results show that laser texturing can significantly inhibit the corrosion of SS310 under such harsh conditions. The main outcomes are.

- Laser texturing process results in the adhesion of long-chain hydrocarbons onto metal surfaces, which decompose at higher temperatures to form protective layers. This process further enhances the corrosion resistance of the treated SS310 samples.
- The untreated samples showed visible signs of pitting and scaling, while minimal surface changes were observed in the treated samples.
- Cross-sectional analysis revealed that the untreated samples experienced considerable peeling compared to a 45% increase in the rate of corrosion observed on the treated samples.
- ICP analysis showed that the concentration of Cr and Mg ions present within the salt was two-fold and four-fold higher in the unprocessed reference LTS (Laser Treated Samples) compared to the processed samples. This indicates that the laser texturing process makes these ions less accessible to the salt, particularly Li, thereby improving the resistance of the material to the corrosive environment.

In conclusion, nanosecond laser micromachining is a highly promising corrosion inhibition strategy for stainless steels in contact with molten carbonate salts, even under dynamic conditions at temperatures and atmospheres close to the salt decomposition. The results of this study highlight the potential of laser texturing as a practical and effective means of mitigating corrosion in the design of components for next-generation CSP plants.

Funding

The work has been performed with the financial support of the National Science Centre (Poland) under Decision No. 2018/31/B/ST8/00599 and through financial support of the HORIZON-MSCA-2021-PF-01 under Grant agreement ID: 101068507.

Intellectual property

We confirm that we have given due consideration to the protection of intellectual property associated with this work and that there are no impediments to publication, including the timing of publication, with respect to intellectual property. In so doing we confirm that we have followed the regulations of our institutions concerning intellectual property.

Authorship

All listed authors meet the “Journal of Solar Energy Materials & Solar Cells” criteria. We attest that all authors contributed significantly to the creation of this manuscript, each having fulfilled criteria as established by the “Journal of Solar Energy Materials & Solar Cells”.

We confirm that the manuscript has been read and approved by all named authors.

We confirm that the order of authors listed in the manuscript has been approved by all named authors.

Contact with the editorial office

We understand that this Corresponding Author is the sole contact for the Editorial process (including direct communications with the office). He/she is responsible for communicating with the other authors about progress, submissions of revisions and final approval of proofs.

We confirm that the email addresses shown below are accessible by the Corresponding Authors, and are the addresses to which Corresponding Authors’s EVISE accounts are linked, and have been configured to accept email from the editorial office of the “Journal of Solar Energy Materials & Solar Cells”.

Table 2
Results of ICP analysis.

Element (ppm)	Cr	Mg	Mn	Ca	Al	Fe	Mo	Zn	Cu	Co	Ni	Sr	Pb
Reference	1.56	0.752	0.08	0.481	0.271	L	L	L	L	L	L	L	L
LTS	0.792	0.025	0.067	0.816	0.18	0.14	0.011	0.06	0.009	0.01	L	L	0.009

All element concentrations were L (below limit of quantification) for the pristine salt.

CRediT authorship contribution statement

Luis González-Fernández: Writing – review & editing, Writing – original draft, Methodology, Investigation, Formal analysis, Data curation. **Argyrios Anagnostopoulos:** Writing – review & editing, Writing – original draft, Investigation, Conceptualization. **Themistoklis Karkantonis:** Writing – review & editing, Methodology, Investigation, Formal analysis. **Stefan Dimov:** Writing – review & editing, Supervision, Investigation. **Mirosław Chorążewski:** Writing – review & editing, Supervision, Investigation. **Yulong Ding:** Writing – review & editing, Supervision, Investigation. **Yaroslav Grosu:** Writing – review & editing, Writing – original draft, Supervision, Methodology, Investigation, Conceptualization.

Declaration of competing interest

Potential conflict of interest exists: No conflict of interest exists.

Data availability

Data will be made available on request.

References

[1] G. San Miguel, B. Corona, Economic viability of concentrated solar power under different regulatory frameworks in Spain, Renew. Sustain. Energy Rev. 91 (2018), https://doi.org/10.1016/j.rser.2018.03.017.

[2] A. Anagnostopoulos, A. Palacios, M.H. Navarro, S. Fereres, Y. Ding, Effect of SiO2 nanoparticle addition on the wetting and rheological properties of solar salt, Sol. Energy Mater. Sol. Cells 210 (2020), 110483, https://doi.org/10.1016/j.solmat.2020.110483.

[3] H. Zarrinkafsh, N. Eslamirad, F. De Luca, Concentrated solar power (CSP) for sustainable architecture to supply domestic hot water and heating loads of buildings, in: J. Phys. Conf. Ser., 2021, https://doi.org/10.1088/1742-6596/2042/1/012110.

[4] W. Ding, J. Gomez-Vidal, A. Bonk, T. Bauer, Molten chloride salts for next generation CSP plants: electrolytical salt purification for reducing corrosive impurity level, Sol. Energy Mater. Sol. Cells 199 (2019), https://doi.org/10.1016/j.solmat.2019.04.021.

[5] N.S. Patel, V. Pavlík, M. Boča, High-temperature corrosion behavior of superalloys in molten salts–A review, Crit. Rev. Solid State Mater. Sci. 42 (2017) 83–97, https://doi.org/10.1080/10408436.2016.1243090.

[6] J. Luo, C.K. Deng, N. ul H. Tariq, N. Li, R.F. Han, H.H. Liu, J.Q. Wang, X.Y. Cui, T. Y. Xiong, Corrosion behavior of SS316L in ternary Li2CO3–Na2CO3–K2CO3 eutectic mixture salt for concentrated solar power plants, Sol. Energy Mater. Sol. Cells 217 (2020), https://doi.org/10.1016/j.solmat.2020.110679.

[7] M. Sarvghad, T.A. Steinberg, G. Will, Corrosion of steel alloys in eutectic NaCl+ Na2CO3 at 700 °C and Li2CO3 + K2CO3 + Na2CO3 at 450 °C for thermal energy storage, Sol. Energy Mater. Sol. Cells 170 (2017) 48–59, https://doi.org/10.1016/J.SOLMAT.2017.05.063.

[8] Y. Grosu, A. Anagnostopoulos, M.E. Navarro, Y. Ding, A. Faik, Inhibiting hot corrosion of molten Li2CO3-Na2CO3-K2CO3 salt through graphitization of construction materials for concentrated solar power, Sol. Energy Mater. Sol. Cells (2020), https://doi.org/10.1016/j.solmat.2020.110650.

[9] X. Zhang, C. Zhang, Y. Wu, Y. Lu, Experimental research of high temperature dynamic corrosion characteristic of stainless steels in nitrate eutectic molten salt, Sol. Energy (2020), https://doi.org/10.1016/j.solener.2020.09.034.

[10] M. Sarvghad, G. Will, T.A. Steinberg, Corrosion of Inconel 601 in molten salts for thermal energy storage, Sol. Energy Mater. Sol. Cells 172 (2017) 220–229, https://doi.org/10.1016/J.SOLMAT.2017.07.036.

[11] T.H. Lim, E.R. Hwang, H.Y. Ha, S.W. Nam, I.H. Oh, S.A. Hong, Effects of temperature and partial pressure of CO2/O2 on corrosion behaviour of stainless-steel in molten Li/Na carbonate salt, J. Power Sources 89 (2000) 1–6, https://doi.org/10.1016/S0378-7753(00)00376-1.

[12] S. Frangini, S. Loreti, The role of temperature on the corrosion and passivation of type 310S stainless steel in eutectic (Li+K) carbonate melt, J. Power Sources 160 (2006) 800–804, https://doi.org/10.1016/j.jpowsour.2006.04.068.

[13] K. Takeuchi, A. Nishijima, K. Ui, N. Koura, C.-K. Loong, Corrosion behavior of Fe-Cr alloys in Li2CO3-K2CO3 molten carbonate, J. Electrochem. Soc. 152 (2005) B364, https://doi.org/10.1149/1.1955168.

[14] Y. Zhang, P. Wang, K. Zheng, H. Yin, D. Wang, Corrosion behaviors of SS310 and IN718 alloys in molten carbonate, J. Electrochem. Soc. 168 (2021), 121510, https://doi.org/10.1149/1945-7111/AC436B.

[15] B. Zhu, G. Lindbergh, Corrosion behaviour of high-chromium ferritic steels in molten carbonate in cathode environment, Electrochim. Acta 46 (2001) 2593–2604, https://doi.org/10.1016/S0013-4686(01)00471-6.

[16] J.P.T. Vossen, L. Plomp, J.H.W. de Wit, G. Rietveld, Corrosion behavior of stainless steel and nickel-base alloys in molten carbonate, J. Electrochem. Soc. 142 (1995) 3327–3335, https://doi.org/10.1149/1.2049983/XML.

[17] M.T. de Miguel, V. Encinas-Sánchez, M.I. Lasanta, G. García-Martín, F.J. Pérez, Corrosion resistance of HR3C to a carbonate molten salt for energy storage applications in CSP plants, Sol. Energy Mater. Sol. Cells 157 (2016) 966–972, https://doi.org/10.1016/j.solmat.2016.08.014.

[18] C.S. Ni, L.Y. Lu, C.L. Zeng, Y. Niu, Electrochemical impedance studies of the initial-stage corrosion of 310S stainless steel beneath thin film of molten (0.62Li, 0.38K) 2CO3 at 650 °C, Corrosion Sci. 53 (2011) 1018–1024, https://doi.org/10.1016/J.CORSCI.2010.11.036.

[19] S.P. Sah, Corrosion of 304 stainless steel in carbonates melt– a state of enhanced dissolution of corrosion products, Corrosion Sci. 169 (2020), 108535, https://doi.org/10.1016/J.CORSCI.2020.108535.

[20] S. Bell, T. Steinberg, G. Will, Corrosion mechanisms in molten salt thermal energy storage for concentrating solar power, Renew. Sustain. Energy Rev. (2019), https://doi.org/10.1016/j.rser.2019.109328.

[21] L. Ma, C. Zhang, Y. Wu, Y. Lu, Comparative review of different influence factors on molten salt corrosion characteristics for thermal energy storage, Sol. Energy Mater. Sol. Cells 235 (2022), https://doi.org/10.1016/j.solmat.2021.111485.

[22] P. Audigié, V. Encinas-Sánchez, S. Rodríguez, F.J. Pérez, A. Agüero, High temperature corrosion beneath carbonate melts of aluminide coatings for CSP application, Sol. Energy Mater. Sol. Cells 210 (2020), https://doi.org/10.1016/j.solmat.2020.110514.

[23] S. Frangini, S. Loreti, The role of alkaline-earth additives on the molten carbonate corrosion of 316L stainless steel, Corrosion Sci. 49 (2007) 3969–3987, https://doi.org/10.1016/j.corsci.2007.05.005.

[24] A. Ibrahim, H. Peng, A. Riaz, M. Abdul Basit, U. Rashid, A. Basit, Molten salts in the light of corrosion mitigation strategies and embedded with nanoparticles to enhance the thermophysical properties for CSP plants, Sol. Energy Mater. Sol. Cells 219 (2021), https://doi.org/10.1016/j.solmat.2020.110768.

[25] U. Nithiyanantham, Y. Grosu, L. González-Fernández, A. Zaki, J.M. Igartua, A. Faik, Development of molten nitrate salt based nanofluids for thermal energy storage application: high thermal performance and long storage components lifetime, in: AIP Conf. Proc., 2019, https://doi.org/10.1063/1.5117740.

[26] Y. Grosu, N. Udayashankar, O. Bondarchuk, L. González-Fernández, A. Faik, Unexpected effect of nanoparticles doping on the corrosivity of molten nitrate salt for thermal energy storage, Sol. Energy Mater. Sol. Cells (2018), https://doi.org/10.1016/j.solmat.2018.01.002.

[27] P. Kondaiah, R. Pitchumani, Fractal textured surfaces for high temperature corrosion mitigation in molten salts, Sol. Energy Mater. Sol. Cells 230 (2021), https://doi.org/10.1016/j.solmat.2021.111281.

[28] P. Kondaiah, R. Pitchumani, Novel textured surfaces for superior corrosion mitigation in molten carbonate salts for concentrating solar power, Renew. Sustain. Energy Rev. 170 (2022), 112961, https://doi.org/10.1016/J.RSER.2022.112961.

[29] Y. Grosu, U. Nithiyanantham, A. Zaki, A. Faik, A simple method for the inhibition of the corrosion of carbon steel by molten nitrate salt for thermal storage in concentrating solar power applications, Npj Mater. Degrad. 2 (2018) 34, https://doi.org/10.1038/s41529-018-0055-0.

[30] Y. Grosu, A. Anagnostopoulos, M.E. Navarro, Y. Ding, A. Faik, Inhibiting hot corrosion of molten salt through graphitization of construction materials for concentrated solar power, Sol. Energy Mater. Sol. Cells 215 (2020), https://doi.org/10.1016/j.solmat.2020.110650.

[31] Á.G. Fernández, L.F. Cabeza, Inhibiting hot corrosion of molten Li<inf>2</inf>CO<inf>3</inf>-Na<inf>2</inf>CO<inf>3</inf>-K<inf>2</inf>CO<inf>3</inf> salt through graphitization of construction materials for concentrated solar power, Sol. Energy Mater. Sol. Cells 194 (2019), https://doi.org/10.1016/j.solmat.2019.02.012.

[32] G. García-Martín, M.I. Lasanta, V. Encinas-Sánchez, M.T. de Miguel, F.J. Pérez, Evaluation of corrosion resistance of A516 Steel in a molten nitrate salt mixture using a pilot plant facility for application in CSP plants, Sol. Energy Mater. Sol. Cells 161 (2017), https://doi.org/10.1016/j.solmat.2016.12.002.

[33] L. Ma, C. Zhang, Y. Wu, Y. Lu, C. Ma, Dynamic corrosion behavior of 316L stainless steel in quaternary nitrate-nitrite salts under different flow rates, Sol. Energy Mater. Sol. Cells 218 (2020), 110821, https://doi.org/10.1016/J.SOLMAT.2020.110821.

[34] A. Mallco, F. Pineda, M. Mendoza, M. Henriquez, C. Carrasco, V. Vergara, E. Fuentealba, A.G. Fernandez, Evaluation of flow accelerated corrosion and mechanical performance of martensitic steel T91 for a ternary mixture of molten salts for CSP plants, Sol. Energy Mater. Sol. Cells 238 (2022), 111623, https://doi.org/10.1016/J.SOLMAT.2022.111623.

[35] L. González-Fernández, A. Anagnostopoulos, T. Karkantonis, O. Bondarchuk, S. Dimov, M. Chorążewski, Y. Ding, Y. Grosu, Laser-induced carbonization of stainless steel as a corrosion mitigation strategy for high-temperature molten salts applications, J. Energy Storage 56 (2022), 105972, https://doi.org/10.1016/J.EST.2022.105972.

[36] L. González-Fernández, M. Intxaurtieta-Carcedo, O. Bondarchuk, Y. Grosu, Effect of dynamic conditions on high-temperature corrosion of ternary carbonate salt for thermal energy storage applications, Sol. Energy Mater. Sol. Cells 240 (2022), https://doi.org/10.1016/J.SOLMAT.2022.111666.

[37] G. García-Martín, M.I. Lasanta, V. Encinas-Sánchez, M.T. de Miguel, F.J. Pérez, Evaluation of corrosion resistance of A516 Steel in a molten nitrate salt mixture using a pilot plant facility for application in CSP plants, Sol. Energy Mater. Sol. Cells 161 (2017) 226–231, https://doi.org/10.1016/J.SOLMAT.2016.12.002.

[38] P. Audigié, V. Encinas-Sánchez, M. Juez-Lorenzo, S. Rodríguez, M. Gutiérrez, F. J. Pérez, A. Agüero, High temperature molten salt corrosion behavior of aluminide and nickel-aluminide coatings for heat storage in concentrated solar power plants, Surf. Coating. Technol. 349 (2018) 1148–1157, https://doi.org/10.1016/J.SURFCOAT.2018.05.081.

[39] D. Huerta-Murillo, A. García-Girón, J.M. Romano, J.T. Cardoso, F. Cordovilla, M. Walker, S.S. Dimov, J.L. Ocaña, Wettability modification of laser-fabricated hierarchical surface structures in Ti-6Al-4V titanium alloy, Appl. Surf. Sci. 463 (2019), https://doi.org/10.1016/j.apsusc.2018.09.012.
[40] J.T. Cardoso, A. Garcia-Girón, J.M. Romano, D. Huerta-Murillo, R. Jagdheesh, M. Walker, S.S. Dimov, J.L. Ocaña, Influence of ambient conditions on the evolution of wettability properties of an IR-, ns-laser textured aluminium alloy, RSC Adv. 7 (2017), https://doi.org/10.1039/c7ra07421b.
[41] W. Wang, B. Guan, X. Li, J. Lu, J. Ding, Corrosion behavior and mechanism of austenitic stainless steels in a new quaternary molten salt for concentrating solar power, Sol. Energy Mater. Sol. Cells 194 (2019) 36–46, https://doi.org/10.1016/j.solmat.2019.01.024.
[42] O. Sotelo-Mazón, C. Cuevas-Arteaga, J. Porcayo-Calderón, V.M. Salinas Bravo, G. Izquierdo-Montalvo, Corrosion behavior of pure Cr, Ni, and Fe exposed to molten salts at high temperature, 2014, Adv. Mater. Sci. Eng. (2014), https://doi.org/10.1155/2014/923271.
[43] M. Keijzer, G. Lindbergh, K. Hemmes, P.J.J.M. Van Der Put, J. Schoonman, J.H. W. De Wit, Corrosion of 304 stainless steel in molten-carbonate fuel cells, J. Electrochem. Soc. 146 (1999) 2508–2516.
[44] K. Takeuchi, A. Nishijima, K. Ui, N. Koura, C.-K. Loong, Corrosion behavior of Fe-Cr alloys in Li[sub 2]CO[sub 3]-K[sub 2]CO[sub 3] molten carbonate, J. Electrochem. Soc. 152 (2005) B364, https://doi.org/10.1149/1.1955168.
[45] H.M. Chung, J.E. Sanecki, F.A. Garner, Radiation-induced Instability of MnS Precipitates and its Possible Consequences on Irradiation-Induced Stress Corrosion Cracking of Austenitic Stainless Steels, ASTM Spec. Tech. Publ., 1999, pp. 647–658, https://doi.org/10.1520/STP13894S.
[46] C.-H. Su, C.-H. Zhang, al - S.J. Rothman, L.J. Nowicki, G.E. Murch, Self-diffusion in austenitic Fe-Cr-Ni alloys, J. Phys. F Met. Phys. 10 (1980) 383, https://doi.org/10.1088/0305-4608/10/3/009.
[47] S. Kamal, K.V. Sharma, P. Srinivasa Rao, O. Mamat, Thermal spray coatings for hot corrosion resistance, Top. Mining, Metall. Mater. Eng. (2017) 235–268, https://doi.org/10.1007/978-3-319-29761-3_10/TABLES/1.
[48] T. Ishitsuka, K. Nose, Stability of protective oxide films in waste incineration environment - solubility measurement of oxides in molten chlorides, Corrosion Sci. 44 (2002) 247–263, https://doi.org/10.1016/S0010-938X(01)00059-2.
[49] S.H. Goods, R.W. Bradshaw, Corrosion of stainless steels and carbon steel by molten mixtures of commercial nitrate salts, J. Mater. Eng. Perform. 13 (2004) 78–87, https://doi.org/10.1361/10599490417542.
[50] S.P. Sah, E. Tada, A. Nishikata, Corrosion behaviour of austenitic stainless steels in carbonate melt at 923 K under controlled CO2-O2 environment, Corrosion Sci. 133 (2018), https://doi.org/10.1016/j.corsci.2018.01.031.
[51] J. Wintterlin, M.L. Bocquet, Graphene on metal surfaces, Surf. Sci. 603 (2009) 1841–1852, https://doi.org/10.1016/J.SUSC.2008.08.037.
[52] S. Ahmed, A. Aitani, F. Rahman, A. Al-Dawood, F. Al-Muhaish, Decomposition of hydrocarbons to hydrogen and carbon, Appl. Catal. Gen. 359 (2009) 1–24, https://doi.org/10.1016/J.APCATA.2009.02.038.
[53] Y. Zhang, D.M. Schleich, Preparation and characterization of iron manganese carbide by reaction of the oxides and carbon in nitrogen, J. Solid State Chem. 110 (1994) 270–273, https://doi.org/10.1006/JSSC.1994.1169.
[54] A.-M. Kietzig, S.G. Hatzikiriakos, P. Englezos, Patterned Superhydrophobic Metallic Surfaces, 2009, https://doi.org/10.1021/la8037582.
[55] M. Gonzalez, U. Nithiyanantham, E. Carbó-Argibay, O. Bondarchuk, Y. Grosu, A. Faik, Graphitization as efficient inhibitor of the carbon steel corrosion by molten binary nitrate salt for thermal energy storage at concentrated solar power, Sol. Energy Mater. Sol. Cells 203 (2019), 110172, https://doi.org/10.1016/j.solmat.2019.110172.
[56] F. Farelas, B. Brown, S. Nesic, /NACECORR/proceedings-abstract/CORR13/All-CORR13/121443, in: Iron Carbide and its Influence on the Formation of Protective Iron Carbonate in CO2 Corrosion of Mild Steel, 2013. (Accessed 22 February 2023).
[57] A.G. Fernández, L.F. Cabeza, Corrosion monitoring and mitigation techniques on advanced thermal energy storage materials for CSP plants, Sol. Energy Mater. Sol. Cells 192 (2019) 179–187, https://doi.org/10.1016/j.solmat.2018.12.028.
[58] A.G. Fernández, H. Galleguillos, E. Fuentealba, F.J. Pérez, Corrosion of stainless steels and low-Cr steel in molten Ca(NO3)2–NaNO3–KNO3 eutectic salt for direct energy storage in CSP plants, Sol. Energy Mater. Sol. Cells 141 (2015) 7–13, https://doi.org/10.1016/J.SOLMAT.2015.05.004.
[59] A.G. Fernández, H. Galleguillos, F.J. Pérez, Thermal influence in corrosion properties of Chilean solar nitrates, Sol. Energy 109 (2014) 125–134, https://doi.org/10.1016/J.SOLENER.2014.07.027.
[60] Z. Sun, Y. Luo, P. Song, X. Gao, Acceleration of thermal decomposition of molten nitrates by Cr in steel and promotion of this effect by halogens, AIChE J. (2022), https://doi.org/10.1002/aic.17905.
[61] L. González-Fernández, A. Anagnostopoulos, T. Karkantonis, O. Bondarchuk, S. Dimov, M. Chorążewski, Y. Ding, Y. Grosu, Laser-induced carbonization of stainless steel as a corrosion mitigation strategy for high-temperature molten salts applications, J. Energy Storage 56 (2022), 105972, https://doi.org/10.1016/J.EST.2022.105972.